

On the Impact of Electromagnetic Interference and Inter-RIS Reflections in Indoor Factory Local 6G Networks

Ishan Rangajith Koralege, Nurul Huda Mahmood, *Member, IEEE*,
and Arthur Sousa de Sena, *Member, IEEE*, Italo Atzeni, *Senior Member, IEEE*

Abstract—The Sixth Generation (6G) radio technology is expected to include local 6G networks as a special use case, extending the capabilities of ‘generic’ 6G networks towards more demanding performance requirements. Reconfigurable intelligent surfaces (RISs) offer a novel paradigm for next-generation wireless communications, especially in the context of local 6G networks, enabling advanced signal propagation control through intelligent phase-shift configurations. However, in practical deployments, their performance can be adversely affected by electromagnetic interference (EMI) from external sources and inter-RIS reflections (IRR) caused by signal reflections between multiple colocated RIS units. This paper presents a comprehensive analysis of the joint impact of EMI and IRR in a multi-RIS multi-cell system deployed within an indoor factory environment. A detailed evaluation study is first carried out to investigate their impact on system performance. System-level simulations demonstrate that the joint impact of EMI and IRR degrades system performance more significantly than their individual effects, particularly as RIS dimensions and transmit power increase. To address these adverse effects, an alternate optimization algorithm using the Riemannian conjugate gradient method is then proposed. The novel algorithm optimizes the phase shifts of the RIS elements considering the spatial correlation among their associated channels, and is found to provide up to several orders of magnitude gains in terms of the system sum rate and the outage probability.

Index Terms—6G, electromagnetic interference (EMI), inter-RIS reflections (IRR), local 6G, phase shift optimization, reconfigurable intelligent surfaces (RIS), Riemannian conjugate gradient (RCG), system-level simulation.

I. INTRODUCTION

The sixth generation (6G) radio technology is expected to support various novel characteristics in terms of operating spectrum, operational range, and served applications. A typical example is the local 6G network paradigm, which operates in spatially constrained service areas such as an indoor factory setting. Local 6G networks pose significant and unique challenges in interference and radio resource management, calling for innovative technological solutions [1].

Reconfigurable intelligent surfaces (RISs) have gained significant attention as a potential enabler in recent years due to their promising capabilities in enhancing the performance of wireless communication systems [2], [3]. An RIS comprises nearly passive reflecting elements capable of intelligently manipulating the wireless propagation environment [4]. Through

The authors are with the Centre for Wireless Communications, University of Oulu, Finland. E-mail: {ishan.koralege, nurulhuda.mahmood, arthur.sena, italo.atzeni}@oulu.fi.

The research leading to this paper was supported by the Research Council of Finland (336449 Profi6, 348396 HIGH-6G, 369116 6G Flagship and 359850 6G-ConCoRSe) and Business Finland’s 6GBridge program (8002/31/2022 Local 6G).

adaptive control of the phase shifts of the RIS elements, the random wireless environment is passively transformed into a controllable channel, thereby rendering the signal propagation more deterministic. This leads to enhanced system performance in terms of signal quality, coverage extension, spectral efficiency, or reduced interference [5].

An RIS is particularly advantageous in local 6G networks like indoor factory environments, which often present complex propagation challenges such as severe multipath fading, signal blockage from heavy machinery, and structural obstacles [4]. In dense indoor factory environments, deploying RISs can effectively address these challenges by overcoming obstacles and mitigating non-line-of-sight (NLoS) conditions, thereby significantly improving system reliability and performance [6].

The potential of RIS as an enabling technology for 6G communication systems depends on several key factors, such as the alignment of the RIS phase shifts and its operation in an interference-free environment. Many existing studies on RISs tend to overlook these practical assumptions, resulting in an inflated performance gain. Hence, it is important to evaluate the performance of an RIS-enabled wireless system under practical system considerations to understand its true potential.

Electromagnetic interference (EMI) represents one of the primary challenges associated with the practical deployment of RISs [7]. EMI comprises uncontrollable wireless signals originating from both human-made and natural sources. Since RIS elements are unable to reflect signals selectively, ambient interference such as EMI are also reflected along with the desired transmitted signal. This is further exacerbated in indoor factory environments as the operation of heavy machinery and other industrial equipment generates EMI [8]. Recent studies have shown that EMI negatively impacts the performance of RIS-aided systems and cannot be neglected, especially as the number of reflecting elements increases [9]. Moreover, due to the close placement of RIS elements, spatial correlation among the associated channels becomes practically unavoidable [10].

In addition, to ensure comprehensive coverage and effectively support distributed users in complex indoor layouts, factories can deploy multiple RIS units close to each other. Due to this close arrangement, signals may reflect from one RIS unit to another before reaching a receiver, leading to inter-RIS reflections (IRR). These reflections should not be neglected, as they can act as additional EMI sources [11]. Therefore, it is also essential to evaluate the impact of IRR on the performance of an RIS-aided wireless system.

The true potential of RIS lies in phase optimization, which involves adjusting the reflection coefficients of the RIS el-

ements to enhance the desired signal and improve overall signal strength and coverage. In multi-user systems, phase optimization can be employed to steer signals toward intended receivers, while interference can be mitigated to a certain extent through interference-aware optimization strategies.

A. Contribution

In a densely obstructed environment, such as an indoor factory, the combined adverse effects of EMI and IRR must be considered to reflect a more realistic scenario. Although previous studies have individually examined these phenomena, to the best of our knowledge, no existing work has considered their coexisting impact. Motivated by this unexplored scenario, this study is the first to investigate the joint impact of EMI and IRR on the performance of an RIS-aided indoor industrial wireless network. Moreover, we propose a novel interference-aware algorithm that optimizes the RIS phase shifts to maximize the signal-to-interference-plus-noise ratio (SINR) using the Riemannian conjugate gradient (RCG) method, effectively overcoming the detrimental impact of EMI and IRR. Our main contributions are summarized as follows:

- We present a comprehensive analysis of how EMI and IRR impact multiple RIS-aided multi-cluster multi-user multiple-input single-output (MISO) downlink systems in quasi-static indoor factory environments. We emphasize that the combined effects of EMI and IRR represent a critical challenge, as RIS can only passively redirect rather than filter or cancel interference, making their joint impact significantly more severe than when each effect is considered in isolation. To capture these effects, system performance is evaluated in terms of the achievable sum rate and outage probability.
- We propose a novel RCG-based alternate optimization (AO) framework to optimize the RIS phase shifts in the presence of EMI and IRR, and we further investigate the phase optimization behavior considering scenarios with and without the knowledge of these interferences. The employment of the RCG method is motivated by its ability to handle the complex circle manifold on which RIS phase optimization lies, while ensuring convergence to a stationary solution with manageable complexity.
- The analysis and proposed optimization framework are extensively validated numerically, considering a diverse set of parameters such as the number of RIS elements, transmit power levels, EMI power levels, and IRR.

The results demonstrate that the adverse effects of EMI and IRR cannot be overlooked, as they significantly degrade the system performance. However, the proposed EMI and IRR-aware RIS phase shift optimization framework is able to compensate for this degradation with varying performance gains under different system assumptions.

B. Notations and Structure of the Paper

Vectors are denoted by bold lower-case letters, while matrices are represented by bold upper-case letters. The Hermitian of a matrix \mathbf{X} is written as \mathbf{X}^H , while the i th entry of a

vector \mathbf{x} as $[\mathbf{x}]_i$, and the (i, j) th entry of a matrix \mathbf{X} as $[\mathbf{X}]_{ij}$. The Hadamard product is denoted by \odot , and the operator $\text{diag}\{\cdot\}$ constructs a diagonal matrix from a given vector. The Euclidean norm is written as $\|\cdot\|_2$, while the magnitude of a scalar is denoted by $|\cdot|$. For optimization, the Riemannian gradient is expressed as $\text{rgrad}\{\cdot\}$ and the standard gradient operator as ∇ . The expectation operator is denoted by $\mathbb{E}\{\cdot\}$, and the modulo operation by $\text{mod}\{\cdot\}$.

The structure of this paper is as follows. Section II summarizes the related work in the literature. Section III introduces the system and channel models, together with the analytical expressions used in the simulation scenarios. The system-level analysis under different interference conditions is presented in Section IV. To address those interferences, an AO framework is proposed in Section V. Based on this framework, comprehensive system-level simulations are carried out in Section VI to assess the overall performance. Finally, conclusions are drawn in Section VII.

II. RELATED WORKS

A. EMI in RIS-Aided Systems

The impact of EMI on the performance of RIS-aided systems has been investigated in a handful of works. The study in [7] introduced a heuristic RIS phase shift optimization aimed at jointly mitigating thermal noise and EMI. The authors highlighted that EMI becomes increasingly critical as the dimensions of the RIS, i.e., the number of RIS elements, increase. Reference [12] developed an EMI cancellation scheme for an RIS-assisted single antenna system, achieving superior performance over benchmark approaches. A multi-user RIS-assisted downlink ultra-reliable low-latency communications system considering spatially correlated RIS channels under EMI and imperfect channel state information assumption was examined in [10].

The uplink spectral efficiency of RIS-aided cell-free massive multiple-input multiple-output (MIMO) systems under EMI with spatially correlated channels was investigated in [13]. In [14], a joint design framework was introduced for RIS-aided communications in the presence of spatially correlated channels and EMI, targeting both channel estimation and spectral efficiency optimization. By formulating both tasks as mean square error minimization problems, the authors developed an optimization algorithm incorporating the diagonally scaled steepest descent method to optimize the RIS phase shifts. The proposed approach demonstrated effectiveness over existing methods across diverse propagation conditions.

The study in [15] explored the impact of EMI on the achievable secrecy performance of RIS-assisted wiretap systems under the influence of practical impairments such as spatially correlated channel, phase shift noise, and the co-existence of direct and indirect links. Their findings have shown that the influence of EMI on secrecy performance is highly dependent on the eavesdropper's ability to suppress or cancel the interference. The authors in [16] analyzed a multi-pair full-duplex RIS-assisted two-way communication system, explicitly considering practical factors such as EMI and hardware impairments. The authors of [17] proposed an efficient

channel estimation strategy for RIS-aided systems affected by EMI and spatial channel correlation. Their optimized RIS configurations achieved significant improvements in channel estimation compared to conventional benchmarks.

B. IRR in RIS-Aided Systems

The existing literature on IRR reveals two prevailing perspectives concerning how these reflections are addressed within the system design. Most studies (e.g., [18]–[22]) assume multiple distributed RISs are deployed to assist in the desired signal transmission from a transmitter to one or more receivers. Hence, they leverage IRR as constructive signal propagation paths, enhancing overall system performance by improving signal strength, coverage, or spectral efficiency. In contrast, a smaller yet significant body of work (e.g., [11], [23], [24]) considers these reflections as sources of interference, emphasizing the need for dedicated mitigation or cancellation strategies.

In [24], the authors investigated an uplink multi-cell non-orthogonal multiple access (NOMA) scenario assisted by multiple RISs strategically placed near base stations and edge users, with explicit consideration of IRR. Their approach achieved lower power consumption compared to other NOMA schemes and RIS deployment strategies. The work in [23] proposed a novel uplink NOMA communication framework for cascaded RIS-assisted systems. To mitigate IRR, an RIS-level successive interference cancellation mechanism was developed, and results showed that the proposed scheme outperformed existing benchmarks in terms of total transmit power. In [11], the authors investigated a multi-user, multi-RIS uplink system that explicitly accounts for IRR, proposing an AO algorithm for joint phase shift and beamforming design. They further showed that, by effectively managing interference among closely deployed RISs, system throughput can be significantly improved, particularly when the number of RISs and reflecting elements is large.

C. RIS Phase Shift Optimization

RIS phase shift optimization is a widely studied topic. Usually, the phase shifts are optimized considering different objective functions, such as the sum rate, SINR, secrecy rate, energy efficiency, and others [25]–[30]. However, only a few of these works incorporate EMI or IRR into the optimization framework, and none address both simultaneously. In the study [24], an AO approach was employed to jointly design the equalizer, transmit power, and RIS phase shift matrix in the presence of IRR. The authors in [23] also considered IRR and developed a power-efficient transmission strategy through AO of equalizers, transmit power, and RIS phase shifts. In [11], the authors adopted AO to jointly optimize the phase shifts of all the RISs and the beamforming vectors for all the users while accounting for IRR. They showed that their optimization framework can effectively mitigate this interference and even exploit IRR to enhance the received signal power at the base station (BS).

In the study [7], phase optimization is done in a single-input-single-output setup in the presence of EMI. The authors

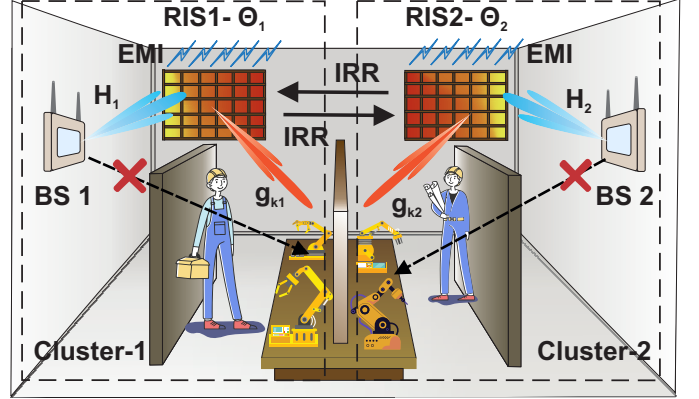


Fig. 1: System model. An indoor factory environment assisted by multiple RISs.

in [14] designed the RIS phase shift coefficients to minimize the mean square error in both channel estimation and data transmission leveraging knowledge of the EMI, proposing an AO framework based on the projected gradient method. Similarly, the study in [31] employed an AO approach that jointly adjusts the beamforming vector and RIS phase shifts to eliminate EMI. In [16], phase shift optimization was carried out in the presence of EMI to maximize the achievable sum rate using a particle swarm optimization algorithm.

III. SYSTEM MODEL

We consider a downlink MISO system in a quasi-static indoor factory environment, where multiple base stations (BSs) serve distributed user equipments (UEs). The UEs are grouped into two clusters, denoted by $n \in \{1, 2\}$ ¹, based on their spatial proximity and communication requirements. Due to dense obstacles in the factory, the direct BS–UE links are often severely blocked. To overcome this limitation and improve coverage, an RIS is strategically deployed in each cluster to enable reliable transmission, as illustrated in Fig. 1. Within each cluster, a BS equipped with T_n antennas serves K_n single-antenna users. The transmitted signal from the BS in the n^{th} cluster is defined as

$$\mathbf{x}_n[m] = \sum_{k=1}^{K_n} \mathbf{u}_{kn} \sqrt{p_{kn}} s_{kn}[m] \quad (1)$$

where $\mathbf{u}_{kn} \in \mathbb{C}^{T_n \times 1}$ denotes the normalized beamforming vector satisfying $\|\mathbf{u}_{kn}\| = 1$, p_{kn} represents the transmit power allocated to the k^{th} user in the n^{th} cluster, and $s_{kn}[m] \in \mathbb{C}$ the normalized data symbol satisfying $\mathbb{E}[|s_{kn}[m]|^2] = 1$. The direct inter-cluster interference is assumed to be negligible due to signal blockage.

Let us assume that each RIS in the n^{th} cluster consists of L_n^2 reflecting elements uniformly arranged in a $L_n \times L_n$ square grid and centered at the origin of its respective coordinate system. The elements of the n^{th} RIS is assumed to have an area

¹The methodologies and formulations developed in this study can be extended to more complex scenarios involving multiple clusters with multiple RISs. Here, we limit the analysis to two clusters for the ease of presentation and to allow drawing meaningful insights.

A_n , and the position of the l^{th} element, indexed row-by-row, is denoted by the coordinate vector $\mathbf{d}_l^{(n)} = [d_{x,l}^{(n)}, d_{y,l}^{(n)}, 0]^T$, where the horizontal and vertical coordinates are given by $d_{x,l}^{(n)} = -(L_n - 1)\frac{\sqrt{A_n}}{2} + \sqrt{A_n} \cdot \text{mod}(l - 1, L_n)$, and $d_{y,l}^{(n)} = (L_n - 1)\frac{\sqrt{A_n}}{2} - \sqrt{A_n} \cdot \lfloor \frac{l-1}{L_n} \rfloor$, where $l \in \{1, 2, \dots, L_n^2\}$. Each RIS element is capable of independently adjusting its reflection amplitude and phase shifts. The matrix of reflection coefficients of the n^{th} RIS is expressed as

$$\Theta_n = \text{diag}(\eta_{n,1} e^{j\varphi_{n,1}}, \eta_{n,2} e^{j\varphi_{n,2}}, \dots, \eta_{n,L_n^2} e^{j\varphi_{n,L_n^2}}), \quad (2)$$

where $\eta_{n,l} \in (0, 1]$ and $\varphi_{n,l} \in [0, 2\pi]$ represent the amplitude and phase of the reflection coefficient associated with the l^{th} element of the n^{th} RIS, respectively. In line with the common assumptions as in [11], to support low-complexity and cost-effective implementations, we set the amplitude of all RIS elements to one. Accordingly, we focus solely on phase shift optimization.

To characterize the path loss between all network components [32], [33], we adopt the 3GPP TR 38.901 LoS path loss model for indoor factory environments with sparse clutter and high base stations (InF-SH) [34]. Accordingly, the path loss coefficient in linear scale for the link $a \in \{\text{BS-UE}, \text{BS-RIS}, \text{RIS-UE}\}$ of the n^{th} cluster is given by

$$\beta_a^{(n)}(d_{3D}) = 31.84 + 21.50 \log_{10}(d_{3D}) + 19.00 \log_{10}(f_c), \quad (3)$$

where d_{3D} denotes the three-dimensional distance in meters and f_c represents the carrier frequency in GHz.

All the channel coefficients are subject to spatially correlated Rayleigh fading. The channel between the BS and the RIS associated with the n^{th} cluster is denoted by $\mathbf{H}_n \in \mathbb{C}^{L_n^2 \times T_n}$, while the channel vector between the RIS and the k^{th} user in the n^{th} cluster is represented by $\mathbf{g}_{kn} = [g_{kn,1}, \dots, g_{kn,L_n^2}]^T \in \mathbb{C}^{L_n^2 \times 1}$, where $k \in \{1, 2, \dots, K\}$. Both \mathbf{H}_n and \mathbf{g}_{nk} are modeled as spatially correlated channels, i.e., $\text{vec}(\mathbf{H}_n) \sim \mathcal{CN}(\mathbf{0}, A_n \beta_{\text{BS-RIS}}^{(n)} \mathbf{I}_{T_n} \otimes \mathbf{R}_n)$ and $\mathbf{g}_{nk} \sim \mathcal{CN}(\mathbf{0}, A_n \beta_{\text{RIS-UE}}^{(n)} \mathbf{R}_n)$. Here, \mathbf{R}_i is the spatial correlation matrix associated with the n^{th} RIS, defined as [7]

$$[\mathbf{R}_n]_{l,\tilde{l}} = \text{sinc} \left(\frac{2\|\mathbf{d}_l^{(n)} - \mathbf{d}_{\tilde{l}}^{(n)}\|}{\lambda} \right), \quad (4)$$

where \mathbf{d}_l and $\mathbf{d}_{\tilde{l}} \in \mathbb{R}^3$ are the positions of the l^{th} and \tilde{l}^{th} elements, respectively, of the n^{th} RIS and λ is the carrier

wavelength. Next, we explore the scenarios influenced by the presence or absence of various types of external interference.

A. Interference Free Scenario in RIS-Aided Networks

We begin by analyzing cluster 1 in isolation, assuming the absence of cluster 2. As a result, IRR is not present in this scenario. Furthermore, we assume that no external EMI sources exist within cluster 1. This setup represents an external interference-free (EIF) scenario. Under these assumptions, the signal received by the k^{th} user in cluster 1 is given by [35]

$$y_{k1}^{\text{EIF}} = \mathbf{g}_{k1}^H \Theta_1 \mathbf{H}_1 \mathbf{x}_1 + n_w, \quad (5)$$

where $n_w \sim \mathcal{CN}(0, \sigma_w^2)$ is the additive white Gaussian noise (AWGN). Then the SINR under the EIF scenario for the k^{th} user is given by

$$\gamma_{k1}^{\text{EIF}} = \frac{p_{k1} |\mathbf{g}_{k1}^H \Theta_1 \mathbf{H}_1 \mathbf{u}_{k1}|^2}{\sum_{i \neq k} p_{i1} |\mathbf{g}_{k1}^H \Theta_1 \mathbf{H}_1 \mathbf{u}_{i1}|^2 + \sigma_w^2}. \quad (6)$$

B. EMI Scenario in RIS-Aided Networks

Let us now analyze cluster 1 in isolation, considering the presence of EMI sources within cluster 1 and assuming that cluster 2 is absent. This assumption effectively eliminates the influence of IRR, thereby simplifying the scenario and enabling a more accurate assessment of the system behavior under the sole influence of EMI. Under this condition, the signal received at the RIS in cluster 1 can be expressed as

$$\mathbf{s} = \mathbf{H}_1 \mathbf{x}_1 + \mathbf{n}_1 \in \mathbb{C}^{L_1^2 \times 1}, \quad (7)$$

where $\mathbf{n}_1 \sim \mathcal{CN}(\mathbf{0}, A_1 \sigma_1^2 \mathbf{R}_1)$ is the EMI at the RIS, with $\mathbb{E}\{\mathbf{n}_1 \mathbf{n}_1^H\} = A_1 \sigma_1^2 \mathbf{R}_1$ and where σ_1^2 is the EMI power. Thus, the received signal under EMI conditions at the k^{th} user in cluster 1 is given by

$$y_{k1}^{\text{EMI}} = \mathbf{g}_{k1}^H \Theta_1 (\mathbf{H}_1 \mathbf{x}_1 + \mathbf{n}_1) + n_w. \quad (8)$$

Using (8), the SINR for the k^{th} user can be derived as in (10) at the bottom of the page.

$$\gamma_{k1}^{\text{EMI}} = \frac{p_{k1} |\mathbf{g}_{k1}^H \Theta_1 \mathbf{H}_1 \mathbf{u}_{k1}|^2}{\sum_{i \neq k} p_{i1} |\mathbf{g}_{k1}^H \Theta_1 \mathbf{H}_1 \mathbf{u}_{i1}|^2 + \mathbf{g}_{k1}^H \Theta_1 A_1 \sigma_1^2 \mathbf{R}_1 \Theta_1^H \mathbf{g}_{k1} + \sigma_w^2}. \quad (10)$$

$$y_{k1}^{\text{IRR}} = \underbrace{\mathbf{g}_{k1}^H \Theta_1 \mathbf{H}_1 \mathbf{u}_{k1} \sqrt{p_{k1}} d_{k1}}_{\text{Desired signal (via RIS 1)}} + \underbrace{\mathbf{g}_{k1}^H \Theta_1 \mathbf{H}_1 \sum_{i \neq k} \mathbf{u}_{i1} \sqrt{p_{i1}} d_{i1}}_{\text{Intra-cluster interference}} + \underbrace{\mathbf{g}_{k1}^H \Theta_1 \mathbf{Z}_{21}^H \Theta_2 \mathbf{H}_2 \sum_{j=1}^N \mathbf{u}_{j2} \sqrt{p_{j2}} d_{j2}}_{\text{IRR via RIS 2 and RIS 1}} + n_w. \quad (11)$$

$$\gamma_{k1}^{\text{IRR}} = \frac{p_{k1} |\mathbf{g}_{k1}^H \Theta_1 \mathbf{H}_1 \mathbf{u}_{k1}|^2}{\sum_{i \neq k} p_{i1} |\mathbf{g}_{k1}^H \Theta_1 \mathbf{H}_1 \mathbf{u}_{i1}|^2 + \sum_{j=1}^N p_{j2} |\mathbf{g}_{k1}^H \Theta_1 \mathbf{Z}_{21}^H \Theta_2 \mathbf{H}_2 \mathbf{u}_{j2}|^2 + \sigma_w^2}. \quad (12)$$

$$\begin{aligned}
y_{k1}^{\text{EMI+IRR}} = & \underbrace{\mathbf{g}_{k1}^H \Theta_1 \mathbf{H}_1 \mathbf{u}_{k1} \sqrt{p_{k1}} d_{k1}}_{\text{Desired signal (via RIS 1)}} + \underbrace{\mathbf{g}_{k1}^H \Theta_1 \mathbf{H}_1 \sum_{i \neq k} \mathbf{u}_{i1} \sqrt{p_{i1}} d_{i1}}_{\text{Intra-cluster interference}} + \underbrace{\mathbf{g}_{k1}^H \Theta_1 \mathbf{Z}_{21}^H \Theta_2 \mathbf{H}_2 \sum_{j=1}^N \mathbf{u}_{j2} \sqrt{p_{j2}} d_{j2}}_{\text{IRR via RIS 2 and RIS 1}} \\
& + \underbrace{2\mathbf{g}_{k2}^H \Theta_1 \mathbf{n}_1}_{\text{Noise reflected by RIS 1}} + \underbrace{\mathbf{g}_{k1}^H \Theta_1 \mathbf{Z}_{21}^H \Theta_2 \mathbf{n}_2}_{\text{Noise from cluster 2 reflected via RIS 2 and RIS 1}} + n_w. \tag{13}
\end{aligned}$$

$$\gamma_{k1}^{\text{EMI+IRR}} = \frac{p_{k1} |\mathbf{g}_{k1}^H \Theta_1 \mathbf{H}_1 \mathbf{u}_{k1}|^2}{\sum_{i \neq k} p_{i1} |\mathbf{g}_{k1}^H \Theta_1 \mathbf{H}_1 \mathbf{u}_{i1}|^2 + \sum_{j=1}^N p_{j2} |\mathbf{g}_{k2}^H \Theta_1 \mathbf{Z}_{21}^H \Theta_2 \mathbf{H}_2 \mathbf{u}_{j2}|^2 + 4\mathbf{g}_{k1}^H \Theta_1 A_1 \sigma_1^2 \mathbf{R}_1 \Theta_1^H \mathbf{g}_{k1} + \dots} \tag{14}$$

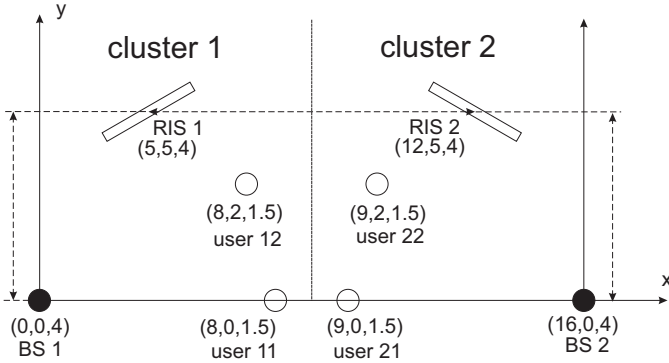


Fig. 2: Simulation Scenario Coordinates.

C. IRR Scenario in RIS-Aided Networks

We now extend the analysis to include both cluster 1 and cluster 2, while focusing on the performance in cluster 1. In the presence of cluster 2, the system is subject to IRR between RIS 1 and RIS 2, which introduces an additional reflection path that must be incorporated into the model. In this scenario, we neglect the effects of EMI within both clusters to isolate and observe the behavior only in the presence of IRR. Under these assumptions, the overall received signal at the k^{th} user in cluster 1 is given by

$$y_{k1}^{\text{IRR}} = \underbrace{\mathbf{g}_{k1}^H \Theta_1 \mathbf{H}_1 \mathbf{x}_1}_{\text{Desired signal}} + \underbrace{\mathbf{g}_{k1}^H \Theta_1 \mathbf{Z}_{21}^H \Theta_2 \mathbf{H}_2 \mathbf{x}_2}_{\text{IRR via RIS 2-RIS 1}} + n_w. \tag{9}$$

where the IRR from the n^{th} RIS in cluster n to the m^{th} RIS in cluster m is given by $\text{vec}(\mathbf{Z}_{nm}) \sim \mathcal{CN}(\mathbf{0}, \sqrt{A_n A_m} \beta_{nm} \mathbf{I}_{L_1^2 L_2^2})$. Here, β_{nm} is the path loss coefficient between the n^{th} RIS and the m^{th} RIS, which follows the same path loss model as in (3). The identity matrix $\mathbf{I}_{L_1^2 \times L_2^2}$ is used under the assumption that spatial correlation between RISs is negligible, as they are designed to serve distinct and sufficiently separated clusters. The received signal in (9) can be further expanded as in (11), leading to the corresponding SINR expressed as in (12) at the bottom of the previous page.

D. Joint Scenario of EMI and IRR in RIS-Aided Networks

Lastly, we consider the combined impact of both EMI and IRR by analyzing the complete system model depicted in Fig. 1. This comprehensive scenario captures the simultaneous

TABLE I: Simulation parameters.

Parameter	Description	Value
f_{c1}, f_{c2}	Carrier frequency	3 GHz
λ_1, λ_2	Wavelength	0.1 m
B	Bandwidth	1 MHz
P_{T2}	Transmit power of BS 2	30 dBm
T_1, T_2	Transmit antennas	2
L_2^2	Elements of RIS 2	400
h_{BS1}, h_{BS2}	Height of BSs	4 m
h_{RIS1}, h_{RIS2}	Height of RISs	4 m
h_{UEs}	Height of UEs	1.5 m

influence of EMI sources within the clusters and the IRR between RIS 1 and RIS 2. As a result, the overall received signal under both EMI and IRR at the k^{th} user in cluster 1 is given by

$$\begin{aligned}
y_{k1}^{\text{EMI+IRR}} = & \underbrace{\mathbf{g}_{k1}^H \Theta_1 (\mathbf{H}_1 \mathbf{x}_1 + \mathbf{n}_1)}_{\text{RIS reflection via RIS 1}} + \underbrace{\mathbf{g}_{k1}^H \Theta_1 (\mathbf{Z}_{21}^H \Theta_2 (\mathbf{H}_2 \mathbf{x}_2 + \mathbf{n}_2) + \mathbf{n}_1)}_{\text{IRR via RIS 2 - RIS 1}} + n_w, \tag{15}
\end{aligned}$$

where $\mathbf{n}_2 \sim \mathcal{CN}(\mathbf{0}, A_2 \sigma_2^2 \mathbf{R}_2)$ is the EMI at the RIS, with $\mathbb{E}\{\mathbf{n}_2 \mathbf{n}_2^H\} = A_2 \sigma_2^2 \mathbf{R}_2$ and where σ_2^2 is the EMI power. Since (15) can be further expanded as in (13), the SINR of the k^{th} user can be expressed as in (14) at the top of the page.

IV. SYSTEM LEVEL ANALYSIS

To investigate the impact of EMI and IRR on the system performance, we conduct a comprehensive system level analysis considering the system setup illustrated in Fig. 1. The proposed approach focuses on evaluating the overall performance of an RIS-aided indoor factory scenario within a multi-cell MISO network topology. In our performance evaluation, we vary the parameters within cluster 1 while keeping all parameters of cluster 2 fixed. For simplicity, each scenario assumes a setup with two antenna BS and two single antenna users, in both clusters, allowing us to observe system behavior in a multi-user environment. We consider a system operating with a thermal noise power spectral density of $N_0 = -174$ dBm/Hz. Consequently, the noise power is calculated as $\sigma_w^2 = N_0 \cdot B = -114$ dBm. The reference area of a reflecting element is $A_1 = A_2 = (\frac{\lambda}{4})^2 = 6.25 \times 10^{-4}$ m 2 . The channels \mathbf{H}_1 , \mathbf{H}_2 and \mathbf{g}_{k1} , \mathbf{g}_{k2} are modeled as isotropic with covariance matrices $R_1 = R_2 = R_{\text{iso}}$. The EMI is also

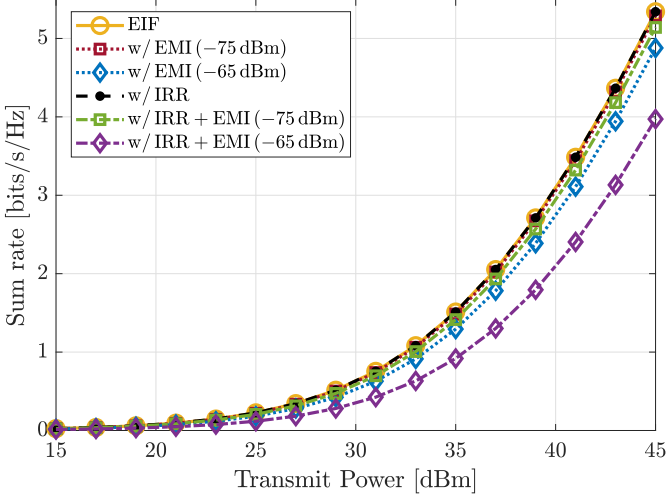


Fig. 3: Sum rate vs transmit power under different interference scenarios.

assumed to be isotropic. The coordinates used in the system-level simulations are illustrated in Fig. 2. Other simulation parameters are summarized in Table I.

The phase shifts of both RISs are fixed to zero; accordingly, the phase shift vectors are set as $\phi_1 = \mathbf{0}_{L_1^2 \times 1}$ and $\phi_2 = \mathbf{0}_{L_2^2 \times 1}$, leading to fixed RIS phase shift matrices $\Theta_1 = \text{diag}(e^{j\phi_1})$ and $\Theta_2 = \text{diag}(e^{j\phi_2})$. Let us assume the interference scenarios EMI, IRR, and the joint EMI and IRR depicted in the system model shown in Fig. 1 and described in Sections III-A, III-B, III-C, and III-D respectively. For the scenarios considering EMI, we are considering two EMI levels as $A_n \sigma_n^2 = -75 \text{ dBm}, -65 \text{ dBm}$. We consider 5×10^3 number of Monte Carlo iterations for each simulation scenario.

A. Variation of Transmit Power with Fixed RIS Elements

In this scenario, we vary the transmit power of BS 1, keeping the number of RIS elements in cluster 1 constant at 400. Fig. 3 illustrates the impact of different interference conditions on sum rate performance versus transmit power. The evaluation scenarios include the EIF case, scenarios with EMI at two different power levels (-75 dBm and -65 dBm), scenarios under IRR, as well as combined conditions involving both IRR and EMI at the two aforementioned EMI power levels. The Fig. 3 clearly shows that the presence of interference significantly affects the system's achievable sum rate. The EIF scenario consistently achieves the highest sum rate across all evaluated transmit power levels, closely followed by the scenario incorporating IRR. The scenario with relatively low EMI (-75 dBm) lies next, displaying moderately reduced performance. However, stronger EMI conditions (-65 dBm) result in a noticeable reduction in sum rate performance. The simultaneous presence of IRR and EMI exhibits a more negative impact on system performance compared to scenarios involving each interference individually. This result clearly highlights the aggregated adverse effect arising from combined interference conditions. The most detrimental impact on performance is given when IRR is combined with stronger EMI.

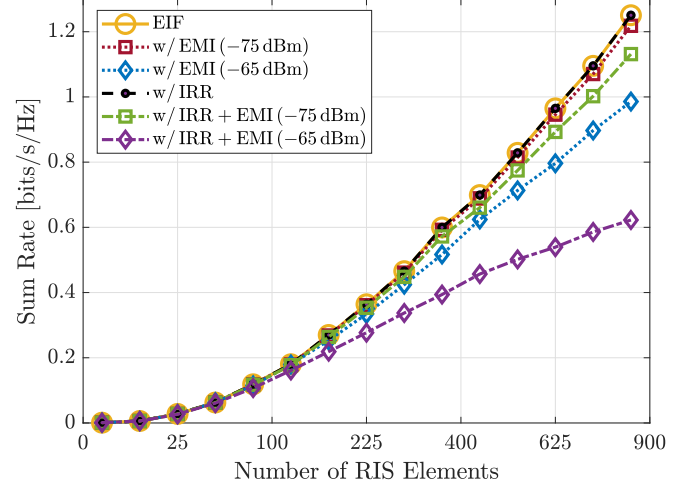


Fig. 4: Sum rate vs number of elements under different interference scenarios.

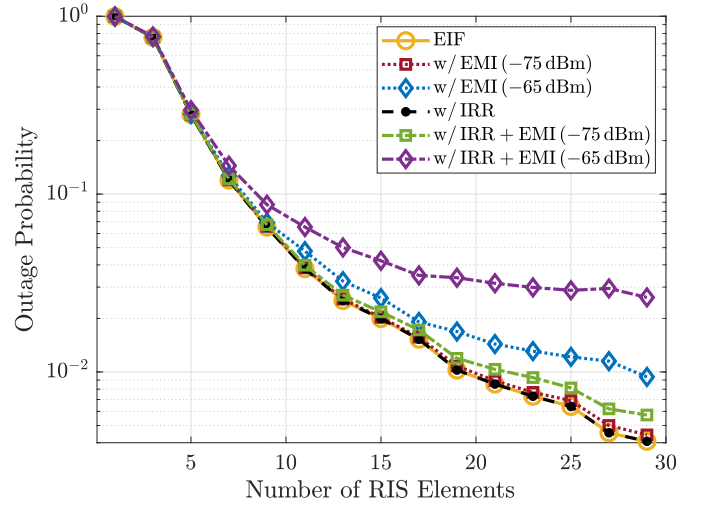


Fig. 5: Outage probability of user 1 vs number of elements under different interference scenarios.

It can be observed that the IRR scenario closely aligns with the EIF scenario. This similarity arises primarily because the impact of IRR, along with other considered conditions, is significantly diminished by the substantial path loss experienced in densely cluttered indoor factory environments. Specifically, in the 3GPP indoor factory path loss model, path loss values already start at approximately 31 dB, further reducing interference effects. These findings also demonstrate the RIS's ability to tolerate moderate levels of interference, effectively mitigating mild adverse effects. Moreover, it can be observed that EMI has a more pronounced impact compared to IRR within indoor factory environments at the given coordinates. As a result, EMI emerges as a dominant limiting factor, emphasizing the importance of strategically managing EMI sources to reduce their emitted power. Notably, the scenario combining both IRR and EMI, particularly at stronger EMI levels, reveals substantial degradation in user reliability, presenting a challenging scenario that critically limits the

capabilities of RISs.

B. Variation of RIS Elements with Fixed Transmit Power

The number of RIS elements in cluster 1 is varied, fixing the transmit power of BS 1 at 30 dBm. Here, the target rate R_{TH} is 0.1 bits/s/Hz. The impact of different interferences on the sum rate and user 1 outage probability is shown by Fig. 4 and Fig. 5, respectively, as a function of the number of RIS elements. Both figures include the EIF scenario, scenarios with two distinct EMI power levels, the scenario involving IRR, and the combined conditions of IRR and EMI at both power levels. Fig. 4 clearly demonstrates that increasing the number of RIS elements consistently improves the sum rate performance across all evaluated scenarios, confirming the effectiveness of RIS in enhancing communication quality by intelligently manipulating the wireless propagation environment. Notably, the EIF scenario achieves the highest sum rate, followed closely by the IRR scenario, with the mild EMI case (-75 dBm) exhibiting further degradation. However, under more severe EMI conditions (-65 dBm), the sum rate drops significantly, underscoring the limitations of RIS effectiveness in the presence of strong interference. The results indicate that weak EMI, when accompanied by IRR, leads to greater performance degradation than weak EMI or IRR in isolation. The negative effect on the sum rate is most significant when IRR is combined with strong EMI at -65 dBm.

The observed results in Fig. 5 distinctly demonstrate that expanding RIS size significantly enhances communication reliability, notably reducing the outage probability across all interference scenarios. In EIF conditions, outage probabilities reach minimal levels, underscoring RIS's remarkable potential for improving link robustness by intelligently controlling signal propagation. The impact of interference, however, becomes particularly significant when evaluating outage probabilities. The IRR scenario, which reflects realistic multi-RIS deployment conditions, exhibits outage probabilities aligned with those of the EIF case. Even mild external multi-user interference (-75 dBm) leads to a noticeable degradation in reliability. In contrast, under stronger EMI conditions (-65 dBm), outage probabilities increase significantly. Moreover, when EMI is combined with IRR, the resulting outage probability exceeds that of their standalone EMI counterparts, indicating a more severe impact on system performance.

V. PROPOSED AO ALGORITHM

Due to the presence of EMI and IRR, a significant degradation in system performance can be observed. To address these impacts, an optimization framework is proposed that jointly optimizes the precoding and RIS phase shifts across three scenarios: EIF, EMI, and joint EMI-IRR. To this end, we consider the weighted sum rate maximization problem for all users, which is formulated in a general mathematical form

applicable to all scenarios as

$$\underset{\mathbf{u}_{k1}, \Theta_1}{\text{maximize}} \quad f(\mathbf{u}_{k1}, \Theta_1) = \sum_{k=1}^{K_1} \omega_k \log(1 + \gamma_{k1}) \quad (16a)$$

$$\text{s.t.} \quad \Theta_1 = \text{diag}(\eta_{1,1} e^{j\varphi_{1,1}}, \dots, \eta_{1,L_1^2} e^{j\varphi_{1,L_1^2}}) \quad (16b)$$

$$|\eta_{1,l}| = 1, \quad \forall l = 1, \dots, L_1^2 \quad (16c)$$

$$\|\mathbf{u}_{k1}\| = 1, \quad \forall k = 1, \dots, K_1. \quad (16d)$$

where ω_k is the weight associated with the k^{th} user. Constraint (16c) enforces the unit-modulus condition on the RIS amplitude coefficients, while constraint (16d) ensures the unit-norm for the precoding vector. This unified problem is then optimized and solved individually for each scenario. The optimization problem in (16) is challenging to solve directly because the objective is non-convex, with SINR terms expressed as ratios of quadratic functions that are coupled with \mathbf{u}_{k1} and Θ_1 . Moreover, the RIS phase-shift variables are constrained to lie on the complex unit circle manifold, which defines a non-convex feasible set. Thus, we adopt an AO framework, where one set of variables is optimized while the other is kept fixed [36]. AO has been extensively adopted in RIS literature and is known to converge to a stationary solution [11], [14], [31], [36]–[38]. In our formulation, when the precoding vector \mathbf{u}_{k1} is fixed, the RIS phase shifts Θ_1 are optimized using the RCG method, which effectively handles the non-convex unit-modulus constraints. Conversely, for fixed RIS phases, the precoding vectors are updated in closed form through the zero-forcing (ZF) solution. The proposed phase optimization is investigated under three different scenarios, and in each case, the AO framework alternates between optimizing the RIS phases and updating the ZF precoding until convergence. Let us now shift our attention to the phase optimization subproblem. For fixed precoding vector \mathbf{u}_{k1} , the sub-problem in Θ_1 is obtained from (16) as

$$\underset{\Theta_1}{\text{maximize}} \quad f(\Theta_1) = \sum_{k=1}^{K_1} \omega_k \log(1 + \gamma_{k1}) \quad (17a)$$

$$\text{s.t.} \quad \Theta_1 = \text{diag}(\eta_{1,1} e^{j\varphi_{1,1}}, \dots, \eta_{1,L_1^2} e^{j\varphi_{1,L_1^2}}) \quad (17b)$$

$$|\eta_{1,l}| = 1, \quad \forall l = 1, \dots, L_1^2. \quad (17c)$$

A. Phase Optimization in the EIF Scenario

We begin by focusing on the EIF scenario in cluster 1 as assumed in Section III-A. In this case, problem (17) can be simplified considering $\gamma = \gamma_{k1}^{\text{EIF}}$ where γ defined as in (6). Based on this simplification, the new optimization problem becomes

$$\underset{\Theta_1}{\text{maximize}} \quad f_{\text{A}}(\Theta_1) = \sum_{k=1}^{K_1} \omega_k \log(1 + \gamma_{k1}^{\text{EIF}}) \quad (18a)$$

$$\text{s.t.} \quad \Theta_1 = \text{diag}(\eta_{1,1} e^{j\varphi_{1,1}}, \dots, \eta_{1,L_1^2} e^{j\varphi_{1,L_1^2}}) \quad (18b)$$

$$|\eta_{1,l}| = 1, \quad \forall l = 1, \dots, L_1^2. \quad (18c)$$

To make the optimization problem more tractable, we further define $\boldsymbol{\theta}_1 = [e^{j\varphi_{1,1}}, \dots, e^{j\varphi_{1,L_1^2}}] = [\theta_{1,1}, \dots, \theta_{1,L_1^2}]^{\text{H}}$, and

$\mathbf{a}_{k1,i} = \text{diag}(\mathbf{g}_{k1}^*) \mathbf{H}_1 \mathbf{u}_{i1} \in \mathbb{C}^{L_1^2 \times 1}$ since we consider a quasi-static indoor scenario. Thus, γ_{k1}^{EIF} can be expressed as

$$\gamma_{k1}^{\text{EIF}} = \frac{p_{k1} |\boldsymbol{\theta}_1^H \mathbf{a}_{k1,k}|^2}{\sum_{i \neq k} p_{i1} |\boldsymbol{\theta}_1^H \mathbf{a}_{k1,i}|^2 + \sigma_w^2}. \quad (19)$$

Therefore, the optimization problem (18) takes the form as

$$\underset{\boldsymbol{\theta}_1}{\text{maximize}} \quad f_B(\boldsymbol{\theta}_1) = \sum_{k=1}^{K_1} \omega_k \log(1 + \gamma_{k1}^{\text{EIF}}) \quad (20a)$$

$$\text{s.t.} \quad |\theta_{1,l}| = 1, \quad \forall l = 1, \dots, L_1^2. \quad (20b)$$

It can be observed that the optimization problem (20) is non-convex. However, the objective function $f_B(\boldsymbol{\theta}_1)$ is continuous and differentiable, and the constraint set defined by $\boldsymbol{\theta}_1$ forms a complex circle manifold. Consequently, a stationary solution to (20) can be effectively obtained via the RCG algorithm [36], which has been widely adopted in RIS-aided communication systems [39]–[41]. During each iteration, the RCG algorithm proceeds through several key steps. First, the Euclidean gradient is computed as

$$\nabla f_B = \sum_{k=1}^{K_1} 2\omega_k \mathbf{a}_k, \quad (21)$$

where

$$\mathbf{a}_k = \frac{\sum_i p_{i1} \mathbf{a}_{k1,i} \mathbf{a}_{k1,i}^H \boldsymbol{\theta}_1}{\sum_i p_{i1} |\boldsymbol{\theta}_1^H \mathbf{a}_{k1,i}|^2 + \sigma_w^2} - \frac{\sum_{i \neq k} p_{i1} \mathbf{a}_{k1,i} \mathbf{a}_{k1,i}^H \boldsymbol{\theta}_1}{\sum_{i \neq k} p_{i1} |\boldsymbol{\theta}_1^H \mathbf{a}_{k1,i}|^2 + \sigma_w^2}. \quad (22)$$

Subsequently, the Riemannian gradient is obtained by projecting the Euclidean gradient ∇f_B onto the tangent space of the complex circle manifold as

$$\text{rgradf}_B = \nabla f_B - \text{Re}\{\nabla f_B \odot \boldsymbol{\theta}_1^*\} \odot \boldsymbol{\theta}_1. \quad (23)$$

Then, the search direction can be determined as

$$\mathbf{d}^{(r)} = \text{rgradf}_B + \tau_1 \mathcal{T}(\mathbf{d}^{(r-1)}). \quad (24)$$

Here τ_1 is the Polak–Ribiere update parameter as [42]

$$\tau_1 = \frac{\text{rgradf}_B^H (\text{rgradf}_B^{(r)} - \text{rgradf}_B^{(r-1)})}{\|\text{rgradf}_B^{(r-1)}\|^2}, \quad (25)$$

and $\mathcal{T}(\cdot)$ denotes the vector transport function, which is defined as

$$\mathcal{T}(\mathbf{d}^{(r)}) = \mathbf{d}^{(r-1)} - \text{Re}\{\mathbf{d}^{(r-1)} \odot \boldsymbol{\theta}_1^*\} \odot \boldsymbol{\theta}_1, \quad (26)$$

where $\mathbf{d}^{(r-1)}$ is the previous search direction. Then, the updated tangent vector is projected back to the complex circle manifold using

$$\theta_{1,l} = \frac{(\theta_{1,l} + \tau_2 \mathbf{d}^{(r)})}{|(\theta_{1,l} + \tau_2 \mathbf{d}^{(r)})|}, \quad \forall l = 1, \dots, L_1^2, \quad (27)$$

where τ_2 is a step size that satisfies the Armijo condition. The complete RCG algorithm for RIS phase optimization, incorporating these steps, is summarized in Algorithm 1, where $\Delta_{\text{Inner}} = |\text{Obj}^{(r)} - \text{Obj}^{(r-1)}|$ and $\text{Obj}^{(r)}$ denotes the weighted sum rate objective value at iteration r . The algorithm iteratively updates the RIS phase vector, starting from an initial

vector $\boldsymbol{\theta}_1^{(0)}$, while keeping the precoding vector \mathbf{u}_{k1} fixed. The convergence threshold ϵ determines when the inner loop terminates.

Algorithm 1 RCG Inner Loop for RIS Phase Optimization

- 1: **Input:** \mathbf{u}_{k1} , $\boldsymbol{\theta}_1^{(0)}$, ϵ , ω_k and parameters required for computing specific γ
- 2: **Output:** Optimized RIS phase vector $\boldsymbol{\theta}_1^{\text{opt}}$
- 3: Initialize $r = 0$ and $\mathbf{d} = 0$
- 4: **repeat**
- 5: Compute the Euclidean gradient using (21) and (22)
- 6: Compute the Riemannian gradient using (23)
- 7: **if** $r = 0$ **then**
- 8: $\mathbf{d} = \text{rgradf}_B$
- 9: **else**
- 10: Compute the update parameter τ_1 as in (25)
- 11: Update search direction \mathbf{d} using (24)
- 12: Perform Armijo line search to determine step size τ_2
- 13: Update $\boldsymbol{\theta}_1^{(r)}$ using (27)
- 14: Evaluate objective: $\text{Obj}^{(r)} \leftarrow f(\boldsymbol{\theta}_1^{(r)})$
- 15: Store $\text{rgradf}_B^{(r-1)} \leftarrow \text{rgradf}_B^{(r)}$, $\mathbf{d}^{(r-1)} \leftarrow \mathbf{d}^{(r)}$
- 16: $r = r + 1$
- 17: **until** $|\Delta_{\text{Inner}}| \leq \epsilon$
- 18: **Return:** $\boldsymbol{\theta}_1^{\text{opt}} \leftarrow \boldsymbol{\theta}_1^{(r)}$

B. Phase Optimization under EMI and IRR

We now assume that cluster 1 is in the presence of EMI as described in section III-B. In line with the previous formulation, we continue by employing the same definition for $\boldsymbol{\theta}_1$, and we define $\mathbf{B} = \text{diag}(\mathbf{g}_{k1}^*) A_1 \sigma_1^2 \mathbf{R}_1 \text{diag}(\mathbf{g}_{k1}) \in \mathbb{C}^{L_1^2 \times L_1^2}$. Thus, γ_{k1}^{EMI} in (10) can be written as

$$\gamma_{k1}^{\text{EMI}} = \frac{p_{k1} |\boldsymbol{\theta}_1^H \mathbf{a}_{k1,k}|^2}{\sum_{i \neq k} p_{i1} |\boldsymbol{\theta}_1^H \mathbf{a}_{k1,i}|^2 + \boldsymbol{\theta}_1^H \mathbf{B} \boldsymbol{\theta}_1 + \sigma_w^2}. \quad (28)$$

Furthermore, considering $\gamma = \gamma_{k1}^{\text{EMI}}$ as defined in (28), problem (17) can be reformulated as follows

$$\underset{\boldsymbol{\theta}_1}{\text{maximize}} \quad f_C(\boldsymbol{\theta}_1) = \sum_{k=1}^{K_1} \omega_k \log(1 + \gamma_{k1}^{\text{EMI}}) \quad (29a)$$

$$\text{s.t.} \quad |\theta_{1,l}| = 1, \quad \forall l = 1, \dots, L_1^2. \quad (29b)$$

When comparing problems (20) and (29), it is evident that they share a similar structure, with the primary distinction arising from the presence of the EMI term in the SINR denominator. Consequently, the same steps in the RCG framework discussed earlier can be applied to obtain a stationary solution. For this modified objective function, the Euclidean gradient can be expressed as follows

$$\nabla f_C = \sum_{k=1}^{K_1} \omega_k \mathbf{b}_k, \quad (30)$$

where

$$\mathbf{b}_k = \frac{2 \sum_i p_{i1} \mathbf{a}_{k1,i} \mathbf{a}_{k1,i}^H \boldsymbol{\theta}_1 + (\mathbf{B} + \mathbf{B}^H) \boldsymbol{\theta}_1}{\sum_i p_{i1} |\boldsymbol{\theta}_1^H \mathbf{a}_{k1,i}|^2 + \boldsymbol{\theta}_1^H \mathbf{B} \boldsymbol{\theta}_1 + \sigma_w^2} - \frac{2 \sum_{i \neq k} p_{i1} \mathbf{a}_{k1,i} \mathbf{a}_{k1,i}^H \boldsymbol{\theta}_1 + (\mathbf{B} + \mathbf{B}^H) \boldsymbol{\theta}_1}{\sum_{i \neq k} p_{i1} |\boldsymbol{\theta}_1^H \mathbf{a}_{k1,i}|^2 + \boldsymbol{\theta}_1^H \mathbf{B} \boldsymbol{\theta}_1 + \sigma_w^2}. \quad (31)$$

Algorithm 2 AO Outer Loop for Joint RIS and Precoding

- 1: **Input:** $\boldsymbol{\theta}_1^{(0)}$, η , ω_k and parameters required for computing \mathbf{u}_{k1} , specific γ
- 2: **Output:** Optimized RIS matrix $\boldsymbol{\Theta}_1^{\text{opt}}$
- 3: Initialize $t = 0$ and $\boldsymbol{\theta}_1 = \boldsymbol{\theta}_1^{(0)}$
- 4: **repeat**
- 5: Compute \mathbf{u}_{k1} using ZF precoder
- 6: For fixed \mathbf{u}_{k1} , optimize $\boldsymbol{\theta}_1$ using Algorithm 1
- 7: Store: $\text{Obj}^{(t)} \leftarrow$ final objective value from Algorithm 1
- 8: $t = t + 1$
- 9: **until** $\Delta_{\text{Outer}} \leq \eta$
- 10: **Return:** $\boldsymbol{\Theta}_1^{\text{opt}} = \text{diag}(\boldsymbol{\theta}_1)$

The same optimization steps outlined in Algorithm 1 can be applied to this scenario by computing the Euclidean gradient using equations (30) and (31), in place of equations (21) and (22) used in the EIF scenario. We now turn our attention to cluster 1 operating under the combined effects of EMI and IRR, as depicted in Fig.1 and described in Section III-D. Similar to the optimization approach for the EIF scenario presented in Section V-A, we optimize the RIS phase shifts in cluster 2 under the assumption that the RIS is unaware of both IRR and EMI. We again adopt the same definition for $\boldsymbol{\theta}_1$ and define $\mathbf{C} = 4 \text{diag}(\mathbf{g}_{k1}^*) \mathbf{A}_1 \sigma_1^2 \mathbf{R}_1 \text{diag}(\mathbf{g}_{k1}) \in \mathbb{C}^{L_1^2 \times L_1^2}$, $\mathbf{D} = \text{diag}(\mathbf{g}_{k1}^*) \mathbf{Z}_{21}^H \boldsymbol{\Theta}_2 \mathbf{A}_2 \sigma_2^2 \mathbf{R}_2 \boldsymbol{\Theta}_2^H \mathbf{Z}_{21} \text{diag}(\mathbf{g}_{k1}) \in \mathbb{C}^{L_1^2 \times L_1^2}$ and $\mathbf{e}_{k1,j} = \text{diag}(\mathbf{g}_{k1}^*) \mathbf{Z}_{21}^H \boldsymbol{\Theta}_2 \mathbf{H}_{21} \mathbf{u}_{j2} \in \mathbb{C}^{L_2^2 \times 1}$. Under these assumptions, and consider $\gamma = \gamma_{k1}^{\text{EMI+IRR}}$ as defined in (34), problem (17) can be presented as follows

$$\underset{\boldsymbol{\theta}_1}{\text{maximize}} \quad f_D(\boldsymbol{\theta}_1) = \sum_{k=1}^{K_1} \omega_k \log(1 + \gamma_{k1}^{\text{EMI+IRR}}) \quad (32a)$$

$$\text{s.t.} \quad |\boldsymbol{\theta}_{1,l}| = 1, \quad \forall l = 1, \dots, L_1^2. \quad (32b)$$

Both problem (29) and (32) share structural similarities apart from the introduction of the additional IRR-related terms in the SINR denominator, as shown in (34) at the bottom of the page.

Therefore, we can again leverage the previously discussed RCG framework to efficiently compute a stationary solution for this scenario as well. The Euclidean gradient corresponding to this modified objective function can be expressed as

$$\nabla f_D = \sum_{k=1}^{K_1} \omega_k \mathbf{c}_k, \quad (33)$$

where \mathbf{c}_k is given as in (35) at the bottom of the page. Similar to the approach described previously, Algorithm 1 can be adapted for this scenario as well by recalculating the Euclidean gradient. Specifically, equations (33) and (35) are used instead of equations (21) and (22), which were originally employed in the EIF scenario.

C. Precoder Optimization

In this work, we adopt ZF precoding given by $\mathbf{u}_{\text{ZF}} = \mathbf{H}_{\text{eff}}^H (\mathbf{H}_{\text{eff}} \mathbf{H}_{\text{eff}}^H)^{-1}$ where the effective channel is given by $\mathbf{H}_{\text{eff}} = \mathbf{g}_{k1}^H \boldsymbol{\Theta}_1 \mathbf{H}_1$. This approach is applied across all clusters and scenarios for consistency and simplicity of implementation and analysis. When $\boldsymbol{\Theta}_1$ is optimized via Algorithm 1, the resulting phase shift values can be directly substituted into the closed-form precoder expressions to obtain the corresponding precoder outputs. In our AO framework, we employ the ZF scheme to compute \mathbf{u}_{k1} for better trackability. The outer loop of the AO is summarized in Algorithm 2, where η is the convergence threshold, $\Delta_{\text{Outer}} = |\text{Obj}^{(t)} - \text{Obj}^{(t-1)}|$.

D. Complexity Analysis

In the proposed AO framework, the optimization alternates between updating the RIS phase vector and the BS precoder. Under the adopted ZF strategy, the precoder update involves constructing the effective cascaded channel matrix and performing a matrix inversion, which incur computational costs of $\mathcal{O}(K_1^2 T_1)$ and $\mathcal{O}(K_1^3)$, respectively. For the RIS phase optimization, the RCG algorithm is employed. The most computationally demanding operation in this procedure is the Euclidean gradient evaluation, which scales as $\mathcal{O}(K_1^2 L_1^4)$. Other steps, such as the Armijo backtracking line search and the retraction operation, require only $\mathcal{O}(K_1^2 L_1^2)$ and $\mathcal{O}(L_1^2)$ computations, respectively, and thus become negligible when L_1^2 is large. By combining these results, the overall computational complexity of the AO algorithm can be expressed as $\mathcal{O}(I_O(K_1^2 T_1 + K_1^3 + I_R K_1^2 L_1^4))$, where I_O and I_R denote the number of outer AO iterations and inner RCG iterations,

$$\gamma_{k1}^{\text{EMI+IRR}} = \frac{p_{k1} |\boldsymbol{\theta}_1^H \mathbf{a}_{k1,k}|^2}{\sum_{i \neq k} p_{i1} |\boldsymbol{\theta}_1^H \mathbf{a}_{k1,i}|^2 + \sum_{j \neq k} p_{j1} |\boldsymbol{\theta}_1^H \mathbf{e}_{k1,j}|^2 + \boldsymbol{\theta}_1^H \mathbf{C} \boldsymbol{\theta}_1 + \boldsymbol{\theta}_1^H \mathbf{D} \boldsymbol{\theta}_1 + \sigma_w^2}. \quad (34)$$

$$\mathbf{c}_k = \frac{2 \sum_i p_{i1} \mathbf{a}_{k1,i} \mathbf{a}_{k1,i}^H \boldsymbol{\theta}_1 + 2 \sum_j p_{j2} \mathbf{e}_{k1,j} \mathbf{e}_{k1,j}^H \boldsymbol{\theta}_1 + (\mathbf{C} + \mathbf{C}^H) \boldsymbol{\theta}_1 + (\mathbf{D} + \mathbf{D}^H) \boldsymbol{\theta}_1}{\sum_i p_{i1} |\boldsymbol{\theta}_1^H \mathbf{a}_{k1,i}|^2 + \sum_j p_{j2} |\boldsymbol{\theta}_1^H \mathbf{e}_{k1,j}|^2 + \boldsymbol{\theta}_1^H \mathbf{C} \boldsymbol{\theta}_1 + \boldsymbol{\theta}_1^H \mathbf{D} \boldsymbol{\theta}_1 + \sigma_w^2} - \frac{2 \sum_{i \neq k} p_{i1} \mathbf{a}_{k1,i} \mathbf{a}_{k1,i}^H \boldsymbol{\theta}_1 + 2 \sum_j p_{j2} \mathbf{e}_{k1,j} \mathbf{e}_{k1,j}^H \boldsymbol{\theta}_1 + (\mathbf{C} + \mathbf{C}^H) \boldsymbol{\theta}_1 + (\mathbf{D} + \mathbf{D}^H) \boldsymbol{\theta}_1}{\sum_{i \neq k} p_{i1} |\boldsymbol{\theta}_1^H \mathbf{a}_{k1,i}|^2 + \sum_{j \neq k} p_{j2} |\boldsymbol{\theta}_1^H \mathbf{e}_{k1,j}|^2 + \boldsymbol{\theta}_1^H \mathbf{C} \boldsymbol{\theta}_1 + \boldsymbol{\theta}_1^H \mathbf{D} \boldsymbol{\theta}_1 + \sigma_w^2}. \quad (35)$$

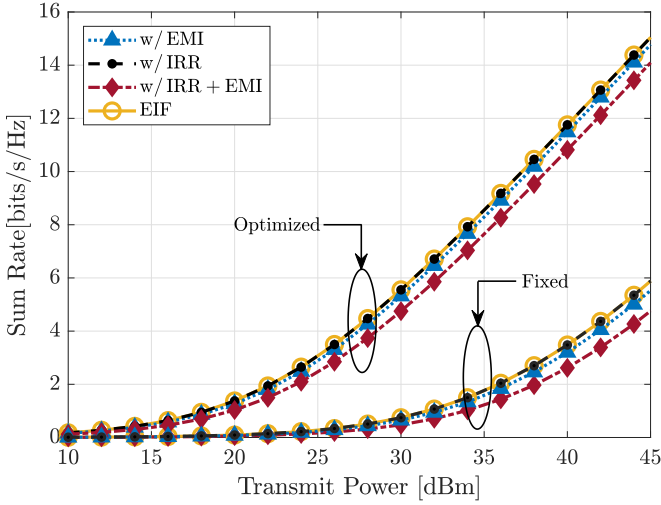


Fig. 6: Sum rate vs transmit power with optimized phase and fixed phase scenarios.

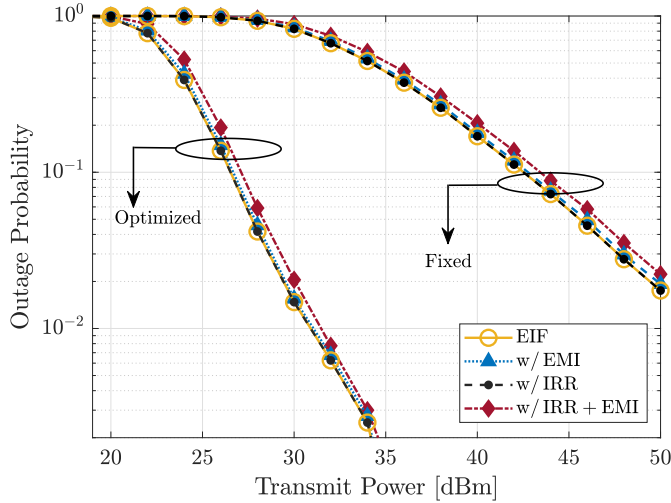


Fig. 7: Outage probability of user 1 vs transmit power under optimized phase and fixed phase scenarios.

respectively. Overall computational complexities calculated for two sets of parameter settings are provided in Table II, assuming $I_O = 10$ and $I_R = 20$.

TABLE II: Computational complexity for different parameter settings.

Setting	K_1	L_1	T_1	Overall Complexity
1	4	64	2	$\mathcal{O}(10(4^2 \times 2 + 4^3 + 20 \times 4^2 \times 64^4)) \approx \mathcal{O}(5.37 \times 10^{10})$
2	8	128	4	$\mathcal{O}(10(8^2 \times 4 + 8^3 + 20 \times 8^2 \times 128^4)) \approx \mathcal{O}(3.44 \times 10^{12})$

VI. PERFORMANCE EVALUATION WITH OPTIMIZED PHASE SHIFTS

In this section, we investigate the optimization of RIS phase shifts under various interference scenarios. Since the RIS demonstrates resilience to low-level interferences, the

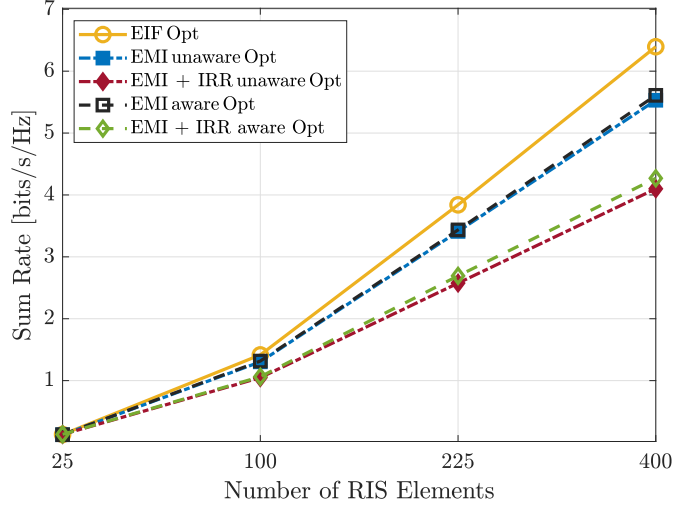


Fig. 8: Sum rate vs number of RIS elements under optimized phase with and without interference knowledge.

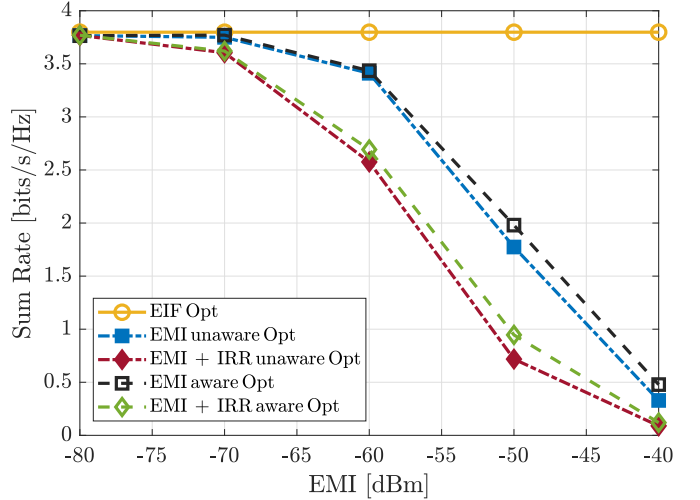


Fig. 9: Sum rate vs EMI power under optimized phase with and without interference knowledge.

phase optimization specifically targeting IRR is omitted as its performance closely overlaps with the EIF scenario. Therefore, our analysis focuses on optimizing RIS phase shifts of cluster 1 with and without the knowledge of EMI and the combined impact of EMI and IRR, and to examine their respective behaviors. For all the scenarios discussed, the phase shifts of the RIS in cluster 2 are optimized following the approach presented in Section V-A, without the knowledge of interferences. Furthermore, an EMI threshold of -60 dBm is adopted in the analysis related to phase shift optimization. To simplify the analysis, we assume that the power is equally allocated among the users, with each user receiving a unit power allocation, and ω_k is considered as one. Initially, the transmit power of cluster 1 is varied, considering an RIS with 225 elements in cluster 1. The corresponding phase shifts are optimized using the algorithm presented in Section V-A, which performs the optimization without incorporating interference knowledge from EMI and IRR. All other system parameters

are as described in Table I. The resulting performance is illustrated in Fig. 6, depicting the sum rate as a function of the transmit power for different interference scenarios with and without phase optimization. We observe a significant improvement of up to 400% in the sum rate with optimized phase shifts across all interference scenarios. The Fig. 7 shows the outage probability of user 1 as a function of the transmit power, with and without RIS phase optimization. Here, the R_{TH} is 0.1 bits/s/Hz. With increasing transmit power, the outage probability decreases for both optimized and fixed RIS configurations. However, the optimized RIS achieves the same outage levels at significantly lower transmit power, and the steeper slope of its curves indicates that RIS optimization leads to a much higher rate of improvement in the outage probability. Optimizing the RIS phase shifts constructively aligns the BS to RIS signal with the signals reflected by the RIS. This improvement increases the overall SINR, thereby enhancing the sum rate and subsequently reducing the outage probability.

Next, we optimize the RIS phase shifts in cluster 1 by incorporating interference knowledge of EMI and IRR, as described in Section V-B. Fig. 8 illustrates the variation of the sum rate with the number of RIS elements in cluster 1, whereas Fig. 9 depicts the impact of different EMI power levels on the sum rate. As shown in Fig. 8, the sum rate increases with the number of RIS elements since a larger number of elements provides more variables to optimize over and enables more reflections that constructively enhance the signal strength and improve the SINR. Since the RIS passively reflects all incident signals, including interferences, both desired and interfering signals experience higher reflection gain as the number of elements increases. Consequently, when EMI and IRR are present, these interference components are also reflected and amplified, causing their impact to intensify with an increasing number of RIS elements. At the same time, the performance gap between the EIF case and the interference-affected cases widens with the increasing number of RIS elements. This occurs because the optimized phase shifts that enhance the desired signal also amplify the interference components, further widening the difference in achievable sum rates.

Fig. 9 indicates a decline in sum rate as EMI power increases. For this scenario, an RIS with 225 elements is used in cluster 1. As EMI gets stronger, the presence of interference knowledge allows the optimization to adjust phase shifts more effectively. As a result, the difference between interference-aware and interference-unaware optimization becomes larger. In both cases, interference-aware optimization consistently outperforms its interference-unaware counterpart. Furthermore, the advantage of interference awareness becomes increasingly significant as the number of RIS elements grows or as the EMI power intensifies. This is because, when interference knowledge is available, the phase optimization process can adaptively address interference effects. A larger RIS provides more controllable elements for phase adjustments when interference knowledge is present. As EMI gets stronger, the availability of interference knowledge enables the RIS to adapt its phase configuration more effectively to address dominant interference.

In all our experiments, we observe that the EIF scenario delivers the highest performance, followed sequentially by the EMI and the combined EMI and IRR scenarios. The combined effect of EMI and IRR results in greater performance degradation compared to EMI alone, since the coexistence of both interference sources amplifies the adverse effects on the received signal and SINR. This trend highlights the system's sensitivity to external interference sources and the importance of incorporating interference awareness in the optimization process. The results confirm that as interference levels increase, adaptive phase shift optimization becomes increasingly crucial to maintain system efficiency. Hence, the proposed AO-based optimization framework demonstrates its capability to address interference and enhance the overall sum rate performance under varying environmental conditions.

VII. CONCLUSION

In this study, we have investigated the practical challenge posed by the joint impact of EMI and IRR on a downlink multi-RIS-aided MISO communication system in local 6G networks, such as an indoor factory environment. Comprehensive system-level simulations demonstrate that ignoring the impact of EMI and IRR, as done in most studies, leads to over-optimistic performance gains. We have shown that in dense, cluttered environments, the combined impact of EMI and IRR leads to a more substantial degradation in system performance than either of their individual counterparts, particularly as the RIS dimensions and transmit power increase.

Furthermore, an EMI and IRR aware AO-based RIS phase shift optimization algorithm is proposed to overcome this performance loss. The proposed AO framework, integrated with the RCG method, provides a clearer understanding of how interference awareness influences the performance of RIS phase shift optimization. The results further demonstrated that the proposed AO approach can effectively mitigate EMI and IRR to some extent. As a future research direction, this study could be extended to scenarios with multiple RISs and to investigate the behaviour of EMI and IRR in the context of beyond-diagonal RIS architectures.

REFERENCES

- [1] P. Ahokangas *et al.*, "Use cases for local 6G networks," in *2024 Joint European Conference on Networks and Communications & 6G Summit (EuCNC/6G Summit)*, Antwerp, Belgium, Jun. 2024, pp. 1127–1132.
- [2] F. Karim and N. H. Mahmood, "An Analysis with interplay of NOMA and RSMA for RIS-aided System," in *2023 Joint European Conference on Networks and Communications & 6G Summit (EuCNC/6G Summit)*, 2023, pp. 162–167.
- [3] I. R. Koralege *et al.*, "A Deep-Unfolding Approach to RIS Phase Shift Optimization via Transformer-Based Channel Prediction," *Scandinavian Simulation Society*, pp. 441–447, 2025.
- [4] N. H. Mahmood *et al.*, "A Functional Architecture for 6G Special-Purpose Industrial IoT Networks," *IEEE Transactions on Industrial Informatics*, vol. 19, no. 3, pp. 2530–2540, 2023.
- [5] S. Dhok *et al.*, "Non-Linear Energy Harvesting in RIS-Assisted URLLC Networks for Industry Automation," *IEEE Transactions on Communications*, vol. 69, no. 11, pp. 7761–7774, 2021.
- [6] S. Ju *et al.*, "142 GHz Sub-Terahertz Radio Propagation Measurements and Channel Characterization in Factory Buildings," *IEEE Transactions on Wireless Communications*, vol. 23, no. 7, pp. 7127–7143, 2024.
- [7] A. de Jesus Torres, L. Sanguinetti, and E. Björnson, "Electromagnetic Interference in RIS-Aided Communications," *IEEE Wireless Communications Letters*, vol. 11, no. 4, pp. 668–672, 2022.

[8] P. Stenumgaard *et al.*, "Challenges and conditions for wireless machine-to-machine communications in industrial environments," *IEEE Communications Magazine*, vol. 51, no. 6, pp. 187–192, 2013.

[9] D. Middleton, "Statistical-Physical Models of Electromagnetic Interference," *IEEE Transactions on Electromagnetic Compatibility*, vol. EMC-19, no. 3, pp. 106–127, 1977.

[10] G. S. Chandra *et al.*, "Downlink URLLC System Over Spatially Correlated RIS Channels and Electromagnetic Interference," *IEEE Wireless Communications Letters*, vol. 11, no. 9, pp. 1950–1954, 2022.

[11] T. V. Nguyen *et al.*, "Leveraging secondary reflections and mitigating interference in multi-IRS/RIS aided wireless networks," *IEEE Transactions on Wireless Communications*, vol. 22, no. 1, pp. 502–517, 2022.

[12] A. Khaleel and E. Basar, "Electromagnetic Interference Cancellation for RIS-Assisted Communications," *IEEE Communications Letters*, vol. 27, no. 8, pp. 2192–2196, 2023.

[13] E. Shi *et al.*, "Uplink Performance of RIS-Aided Cell-Free Massive MIMO System With Electromagnetic Interference," *IEEE Journal on Selected Areas in Communications*, vol. 41, no. 8, pp. 2431–2445, 2023.

[14] W.-X. Long *et al.*, "MMSE Design of RIS-Aided Communications With Spatially-Correlated Channels and Electromagnetic Interference," *IEEE Transactions on Wireless Communications*, vol. 23, no. 11, pp. 16992–17006, 2024.

[15] J. David Vega-Sánchez, G. Kaddoum, and F. J. López-Martínez, "Physical Layer Security of RIS-Assisted Communications Under Electromagnetic Interference," *IEEE Communications Letters*, vol. 26, no. 12, pp. 2870–2874, 2022.

[16] S. R. Kudumala *et al.*, "Hardware Impaired RIS Assisted Multipair FD Communication With Spatial Correlation," *IEEE Communications Letters*, vol. 26, no. 9, pp. 2200–2204, 2022.

[17] Ö. T. Demir, E. Björnson, and L. Sanguinetti, "Efficient Channel Estimation With Shorter Pilots in RIS-Aided Communications: Using Array Geometries and Interference Statistics," *IEEE Transactions on Wireless Communications*, vol. 24, no. 1, pp. 462–478, 2025.

[18] R. Liang *et al.*, "A multi-route cascaded IRSs beamforming scheme for mmWave communication systems," *IEEE Transactions on Vehicular Technology*, vol. 71, no. 6, pp. 6813–6818, 2022.

[19] H. Niu *et al.*, "Double intelligent reflecting surface-assisted multi-user MIMO mmWave systems with hybrid precoding," *IEEE Transactions on Vehicular Technology*, vol. 71, no. 2, pp. 1575–1587, 2021.

[20] Y. Han *et al.*, "Double-IRS aided MIMO communication under LoS channels: Capacity maximization and scaling," *IEEE Transactions on Communications*, vol. 70, no. 4, pp. 2820–2837, 2022.

[21] P. Zhang, S. Gong, and S. Ma, "Double-RIS aided multi-user MIMO communications: Common reflection pattern and joint beamforming design," *IEEE Transactions on Vehicular Technology*, vol. 73, no. 3, pp. 4418–4423, 2023.

[22] X. Ma *et al.*, "Multi-hop multi-RIS wireless communication systems: Multi-reflection path scheduling and beamforming," *IEEE Transactions on Wireless Communications*, vol. 23, no. 7, pp. 6778–6792, 2023.

[23] H. Wang *et al.*, "RIS-level SIC for uplink cascaded-RIS assisted NOMA system," *IEEE Communications Letters*, vol. 27, no. 7, pp. 1884–1888, 2023.

[24] L. Liu, H. Wang, and R. Song, "Optimization for Multi-Cell NOMA Systems Assisted by Multi-RIS With Inter-RIS Reflection," *IEEE Communications Letters*, vol. 28, no. 1, pp. 123–127, 2023.

[25] Z. Peng *et al.*, "Beamforming Optimization for Active RIS-Aided Multiuser Communications With Hardware Impairments," *IEEE Transactions on Wireless Communications*, vol. 23, no. 8, pp. 9884–9898, 2024.

[26] J. Wang *et al.*, "RIS-Aided MIMO Systems With Hardware Impairments: Robust Beamforming Design and Analysis," *IEEE Transactions on Wireless Communications*, vol. 22, no. 10, pp. 6914–6929, 2023.

[27] Z. Sui *et al.*, "Performance Analysis and Optimization of STAR-RIS-Aided Cell-Free Massive MIMO Systems Relying on Imperfect Hardware," *IEEE Transactions on Wireless Communications*, vol. 24, no. 4, pp. 2925–2939, 2025.

[28] C. Huang *et al.*, "Reconfigurable Intelligent Surfaces for Energy Efficiency in Wireless Communication," *IEEE Transactions on Wireless Communications*, vol. 18, no. 8, pp. 4157–4170, 2019.

[29] M.-M. Zhao *et al.*, "Secrecy Rate Maximization of RIS-Assisted SWIPT Systems: A Two-Timescale Beamforming Design Approach," *IEEE Transactions on Wireless Communications*, vol. 22, no. 7, pp. 4489–4504, 2023.

[30] N. Ginige *et al.*, "Max-Min Fairness for Stacked Intelligent Metasurface-Assisted Multi-User MISO Systems," *IEEE Open Journal of the Communications Society*, vol. 6, pp. 5639–5656, 2025.

[31] Y. Ma *et al.*, "Physical-Layer Attack Detection and Countermeasures for RIS-Assisted MIMO Systems," *IEEE Wireless Communications Letters*, vol. 13, no. 1, pp. 123–127, 2024.

[32] T. Jiang *et al.*, "3GPP Standardized 5G Channel Model for IIoT Scenarios: A Survey," *IEEE Internet of Things Journal*, vol. 8, no. 11, pp. 8799–8815, 2021.

[33] S. Ju and T. S. Rappaport, "Statistical Channel Model of Wideband Sub-THz Radio Propagation in Indoor Factories at 142 GHz: Toward 6G Industrial Wireless Networks," *IEEE Transactions on Wireless Communications*, vol. 23, no. 11, pp. 16316–16331, 2024.

[34] 3GPP, "Technical Specification Group Radio Access Network; Study on channel model for frequencies from 0.5 to 100 GHz," 3rd Generation Partnership Project (3GPP), Technical Report TR 38.901 V16.1.0, Dec. 2019, release 16.

[35] C. Huang *et al.*, "Reconfigurable Intelligent Surfaces for Energy Efficiency in Wireless Communication," *IEEE Transactions on Wireless Communications*, vol. 18, no. 8, pp. 4157–4170, 2019.

[36] H. Guo *et al.*, "Weighted Sum-Rate Maximization for Reconfigurable Intelligent Surface Aided Wireless Networks," *IEEE Transactions on Wireless Communications*, vol. 19, no. 5, pp. 3064–3076, 2020.

[37] Q. Wu and R. Zhang, "Intelligent Reflecting Surface Enhanced Wireless Network via Joint Active and Passive Beamforming," *IEEE Transactions on Wireless Communications*, vol. 18, no. 11, pp. 5394–5409, 2019.

[38] C. Huang *et al.*, "Reconfigurable Intelligent Surfaces for Energy Efficiency in Wireless Communication," *IEEE Transactions on Wireless Communications*, vol. 18, no. 8, pp. 4157–4170, 2019.

[39] E. Shtaiwi *et al.*, "Sum-rate maximization for RIS-assisted integrated sensing and communication systems with manifold optimization," *IEEE Transactions on Communications*, vol. 71, no. 8, pp. 4909–4923, 2023.

[40] M. Misbah *et al.*, "Phase and 3-D placement optimization for rate enhancement in RIS-assisted UAV networks," *IEEE Wireless Communications Letters*, vol. 12, no. 7, pp. 1135–1138, 2023.

[41] W. D. S. Junior *et al.*, "Manifold-Based Optimizations for RIS-Aided Massive MIMO Systems," *IEEE Open Journal of the Communications Society*, vol. 5, pp. 7913–7940, 2024.

[42] P.-A. Absil, R. Mahony, and R. Sepulchre, *Optimization Algorithms on Matrix Manifolds*. Princeton, NJ: Princeton University Press, 2008.